Sarajchi, Mohammadhadi and Sirlantzis, Konstantinos (2023) *Pediatric Robotic Lower-Limb Exoskeleton: An Innovative Design and Kinematic Analysis.* IEEE Access, 11 . pp. 115219-115230. ISSN 2169-3536.

RESEARCH ARTICLE

Pediatric Robotic Lower-Limb Exoskeleton: An Innovative Design and Kinematic Analysis

MOHAMMADHADI SARAJCHI[1,2], **(Student Member, IEEE), AND KONSTANTINOS SIRLANTZIS**[2]
[1]School of Engineering, University of Kent, CT2 7NT Canterbury, U.K.
[2]School of Engineering, Technology and Design, Canterbury Christ Church University, CT1 1QU Canterbury, U.K.

Corresponding author: Mohammadhadi Sarajchi (MS2209@kent.ac.uk)

ABSTRACT Lower-limb exoskeletons enhance motor function in patients, benefiting both clinical rehab and daily activities. Nevertheless, pediatric exoskeletons remain largely underdeveloped. To address this gap, this study presents a new robotic lower-limb exoskeleton (LLE) design specifically tailored for children. Utilizing anthropometric data from the target demographic, the LLE has a size-adjustable design to accommodate children aged 8 to 12. The design incorporates six active joints at the hip and knee, actuated using Brushless DC motors in conjunction with Harmonic Drive gears. This study conducts a rigorous analysis of forward and inverse kinematics applied to the robotic LLE. While forward kinematics are essential for dynamic modeling and model-based control formulation, inverse kinematics play a crucial role in facilitating balance control. The study uses an algebraic-geometric method to solve the inverse kinematics of LLEs with four DOFs per leg, including one in the frontal plane and three in the sagittal plane. A unique model of validation and verification is then employed using the Simulink® and Simscape™ computational environments. The accuracy of the forward kinematic analysis is confirmed by comparing separately modeled outcomes in both environments. The validity of the inverse kinematic model is verified by implementing sequential forward and inverse kinematic analyses, comparing the forward kinematic inputs with inverse kinematic outputs. Simulation results conclusively validate both the forward and inverse kinematic analyses, suggesting the exoskeleton's potential in accommodating standard gait patterns.

INDEX TERMS Forward kinematics, inverse kinematics, kinematic analysis, lower-limb exoskeleton, wearable robotics.

I. INTRODUCTION

Motor dysfunction in children is often linked to neurological or neuromuscular disorders, including but not limited to cerebral palsy (CP), muscular dystrophy (MD), spinal muscular atrophy (SMA), and spinal cord injuries (SCI) [1]. CP, the leading mobility disorder in children, is a persistent set of movement disorders stemming from brain injury or damage before birth or during early childhood, with an incidence rate ranging from 1 to nearly 4 per 1,000 live births [2], [3], [4]. MDs are chronic disorders that progressively weaken muscles

The associate editor coordinating the review of this manuscript and approving it for publication was Yangmin Li.

and reduce activity. Duchenne muscular dystrophy (DMD) is the most common of the nine primary types in childhood, affecting 1 in 5,000 [5]. SMA, characterized by spinal cord degeneration and muscle atrophy, is the second most common fatal autosomal recessive disorder after cystic fibrosis [6]. Its incidence is 1 in 6,000 to 1 in 10,000 live births [7]. In the pediatric population, SCI is relatively rare, comprising approximately less than 4% of total annual SCI cases, yet it exerts considerable psychological and physiological effects [8].

These neurological disorders can profoundly affect children's mobility, functional independence, and overall quality of life [9], [10]. Moreover, as they grow, the influence

on motor skill development will increasingly become more pronounced [11]. Although no medical cure exists for these diseases, compelling evidence indicates that the use of powered assistance through wearable robotic LLEs can significantly improve gait efficiency in individuals affected by these impairments [12], [13], [14], [15]. Recently, several single-joint pediatric exoskeletons have been prototyped, but research and development on full lower-limb structures with multiple actuated joints for children are still comparatively neglected in the field [14].

Kinematic analysis plays a fundamental role in understanding the motion of LLEs and their interaction with the human body [16]. In particular, misalignment or kinematic inconsistencies between user and exoskeleton joints may result in unintended human-robot interaction torques. This scenario emphasizes the need for a detailed kinematic analysis of LLEs, particularly for children with neurological disorders [17], [18], [19], [20]. Comprehensive kinematic analysis can guide the optimization of LLE design to cater specifically to the movement patterns and needs of children with neurological disorders. The apt support and assistance provided by such tailored devices can potentially enhance the mobility, functionality, and overall quality of life of these children [21]. Despite these benefits, the contribution of kinematic analysis to the evolution of this technology often remains underappreciated [22]. Moreover, a thorough validation or verification of kinematic analyses is frequently missing in existing LLE literature. This highlights a research gap in the field of LLE technology, necessitating further exploration.

Zhang et al. [23] utilized the Denavit-Hartenberg (D-H) convention for forward kinematic analysis on an LLE, considering each leg fully independent with 5 DOFs. Additionally, they employed an algebraic approach to derive the LLE's inverse kinematic model. However, the model-free nature of the controller in this study precluded the validation of kinematic analysis accuracy, and no separate validation was provided [23]. Lyu et al. [24] conducted forward and inverse kinematics analyses on a three-DOF LLE, simulating the robot's workspace using MATLAB®. However, their study did not include validation for the kinematic analysis. Li et al. [25] conducted an analysis of both forward and inverse kinematics for a three-DOF LLE. They simulated the LLE using ADAMS™; however, their findings lacked subsequent kinematic validation. Zhang et al. [26] conducted forward and inverse kinematic analysis for each leg of a full LLE. However, forward kinematics were individually derived for each plane, specifically the frontal and sagittal planes, and the derived inverse kinematics were not subsequently verified.

This paper aims to bridge the existing research gap concerning the validation and verification of kinematic analyses in LLE literature. The innovative contributions of the paper are: (i) the introduction of a unique pediatric size-adjustable hip-knee-ankle-foot exoskeleton with six actuated joints; (ii) an exhaustive kinematic analysis of the LLE;

(iii) the presentation of a detailed algebraic-geometric solution for the inverse kinematics of the LLE; (iv) the employment of an innovative model validation and verification strategy using the Simulink® and Simscape™ computational environments. This work paves the way toward establishing a robust and scientifically grounded framework for the development and control of wearable robotics for pediatric rehabilitation.

II. THE PEDIATRIC LOWER-LIMB EXOSKELETON

This section introduces a novel pediatric LLE that assists children's lower limb movement, facilitating a stable gait pattern. This prototype is designed with the versatility to accommodate a broad height range from 1.15 m to 1.48 m, rendering it suitable for children aged 8 to 12 years old. The adjustability ensures a quick adaptation to individual user needs. Fig. 1 shows the prototype of this assistive device in the stand mode.

FIGURE 1. Prototype of the LLE in stance position.

A. MECHANICAL DESIGN

This assistive device is equipped with 4 DOFs per leg, of which the frontal hip, sagittal hip, and knee joints are actuated, and the ankle joint is passive. Children between the ages of 6 and 12 undergo significant changes in body size. An anthropometric reference data analysis was undertaken to develop an LLE tailored for pediatrics [27], [28]. The LLE design was based on the extensive anthropometric data outlined in Table 1, accommodating a wide range of the target population. The table summarizes the average body dimensions for children aged 8 to 12, including both girls and boys, at the 50th percentile [28], [29]. This table also delineates the maximum and minimum dimensions of the LLE, providing insight into how the exoskeleton accommodates the target population's physical proportions.

The LLE, crafted from durable and lightweight materials such as aluminum tubes, incorporates telescopic cylinder

TABLE 1. Average body dimensions of children at the 50th percentile, complemented by the maximum and minimum dimensions of the LLE [28], [29].

Type	Children		Exoskeleton	
Gender	Girls	Boys	–	–
Age (years)	8	12	min.	MAX.
H (cm)	123.6±5.6	141±6.9	115	148
LL (cm)	71.9±3.9	84.5±4.7	65	91
ULL (cm)	31.9±1.8	39.1±2.1	29	42
LLL (cm)	40.0±2.1	45.4±2.6	36	49
FL (cm)	18.6±1.2	21.4±1.2	23.5	23.5

H: Height, LL: Leg Length, FL: Foot Length, ULL: Upper Leg Length, LLL: Lower Leg Length.

mechanisms for size adjustability and alignment assurance between user and exoskeleton joints (Fig. 1). A vertical cut was made at one end of the outer tube, with a clamp affixed to the exterior, facilitating convenient length adjustment. The incorporation of quick-release skewers further streamlines and simplifies the adjustment process. These mechanisms, present on both the upper and lower leg sections, grant maximum adaptability across a wide user range and guarantee the provision of the appropriate support level.

B. ACTUATION UNIT

The joint actuation unit is assembled with a 24V brushless DC motor (EC-flat, Maxon Motor AG, Switzerland) and a strain wave gearing system (CPU-17A-M, Harmonic Drive® AG, Germany). Maxon EPOS4 50/15 controllers, functioning as slaves in the network and supporting the EtherCAT protocol, are selected as the drivers for each motor. The configuration of the actuation unit for the three actuated joints is detailed in Table 2. The table demonstrates that each of the three actuation units is capable of achieving the maximum power, torque, and velocity, as specified in the literature related to pediatric gait analysis [14], [26], [30], [31].

TABLE 2. Actuation unit configuration for each joint.

Actuated Joint	Weight (kg)	Pow. Rate (W)	Reduction Ratio	Max. Tor. (Nm)	Max. Vel. (deg/s)
Hip (A/A)	0.35	150	80:1	112	450
Hip (F/E)	0.624	220	100:1	150	300
Knee (F/E)	0.35	150	50:1	70	720

C. SENSORY SYSTEM

The LLE system incorporates an array of sensors, such as hall sensors, absolute encoders, pressure sensors, and IMUs, to enhance its functionality.

Hall sensors, providing real-time feedback on motor position and speed, enable optimal joint movement control, mitigating spasticity by offering consistent motion patterns. The controller, responsive to this feedback, dynamically adjusts exoskeleton assistance, further reducing spasticity potential. Each actuated joint is equipped with a magnetic

absolute rotary encoder, specifically the high-resolution RLS AksIM-2™magnetic encoder, for accurate joint angle measurements. This encoder is connected to the Maxon EPOS4 motor driver using the SSI protocol, ensuring system operation precision. The encoder, serving as the primary sensor, measures the gearbox output angular position, while the hall sensor, acting as a supplementary sensor, captures the motor output angular position.

The exoskeleton's foot is integrated with a sensor board that monitors foot orientation and ground reaction force. It employs four FlexiForce A201 sensors to accurately measure multidirectional pressure distribution. The small output signals from force-sensitive resistors (FSRs) are amplified through four LF356 op-amp microchips. This enables an STM32 Nano microcontroller to efficiently process and transmit the signals using a high-speed CAN bus. Foot orientation is detected by an integrated IMU (MPU9250) located on the electronic board of the foot. An EasyCAT EtherCAT Shield is utilized to gather sensory information from both feet through the CAN bus and actuator signals from a series of EPOS4 drivers. It then facilitates transmission via EtherCAT cable to the central controller (EtherCAT Master), streamlining communication within the system.

D. CONTROLLER ARCHITECTURE

The LLE control system, ensuring precise motor control and real-time sensor data collection, consists of three main components (Fig. 2): local controllers (EtherCAT Slaves), a sensory and communication system, and a central controller (EtherCAT Master).
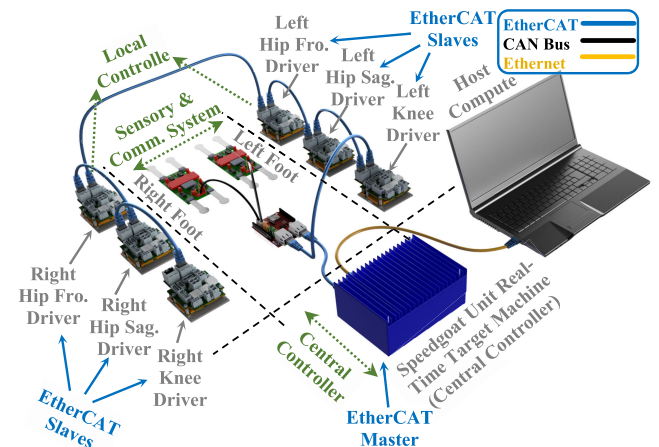
FIGURE 2. Control system configuration and communication architecture of the LLE.

The local controllers provide low-level actuator control on Maxon Epos4 drivers under the EtherCAT protocol. The sensory and communication system interfaces with local controllers via EtherCAT and FSRs via CAN Bus, relaying data and control signals. A compact and high-performance embedded controller (Unit real-time target machine, Speedgoat, Switzerland) has been chosen as the

central control unit to ensure system stability and optimize performance within the LLE.

The Speedgoat Unit real-time target machine, operating at a 1 kHz execution frequency, facilitates the design and development of control algorithms in MATLAB Simulink®. It enables testing without the risk of hardware damage or causing user discomfort, utilizing hardware-in-the-loop (HIL) simulation. Its compatibility with MATLAB, multiple control loops, and sensor input management aid in effectively synchronizing sensors and actuators. Utilizing a user-friendly interface supported by a high-performance Host Computer, the system provides personalized assistance to individual children. In this context, the Speedgoat real-time target machine plays a pivotal role in enabling the creation of more effective, tailored, and responsive assistive devices for patients.

III. FORWARD KINEMATICS

Forward kinematics employs segment lengths and joint angles to compute the end-effector's orientation and position, such as the foot, relative to the origin. This process translates the motion of the exoskeleton's joints into foot movement, allowing for precise control and observation of gait patterns [32], [33]. Forward kinematic analysis not only provides designers with an in-depth understanding of the robotic exoskeleton's motion, but also facilitates the effective use of transformation matrices in developing an explicit dynamic model. This, in turn, leads to the establishment of a model-based controller for the LLE [17], [33], [34], [35].

While the Denavit-Hartenberg (D-H) convention is commonly employed to derive forward kinematics [36], it is unsuitable for the LLE system in this study. This inapplicability stems from the Y-axis rotation between the frontal and sagittal hip joints, which presents a challenge for the conventional D-H approach. Therefore, a conventional approach utilizing the rotation matrix and translation vector is employed to analyse the forward kinematics of the LLE system. This analysis leads to the derivation of the position and orientation of the foot end-effector relative to the origin. Considering that the origin is placed in the frontal plane between the two legs, and each leg operates independently, we have conducted forward kinematics for each leg separately to enhance clarity and ease of understanding.

A. RIGHT LEG

The cartesian coordinate frames assigned to the right leg of the LLE have been presented in Fig. 3A, while Fig. 3B illustrates the simplified model dimensions of the right leg. In Fig. 3B, θ_{iR} and d_i denote the angle and offset of the i-th joint, respectively, and a_i indicates the length of the i-th link. This Fig. demonstrates that coordinate frame 1 (O_{1R}) has undergone a 90-degree rotation around the Y-axis, followed by a -90-degree rotation around the Z-axis. The homogeneous
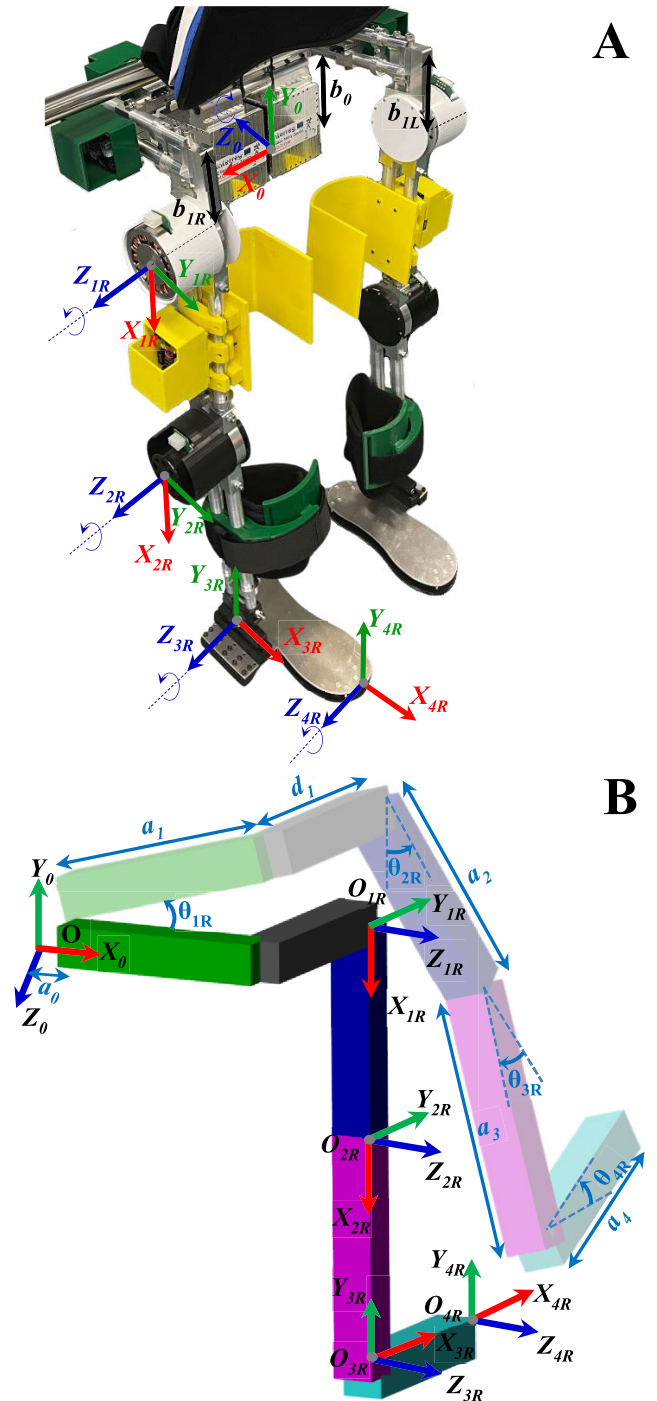

FIGURE 3. Forward kinematic analysis of the right leg of the LLE. (A) The right leg of the LLE with assigned Cartesian coordinate frames. (B) Dimensions of the simplified model of the right leg of the LLE.

transformation matrices for the right leg of the LLE are:

$$T_0^{1R} = \begin{bmatrix} cos(\frac{\pi}{2} - \theta_{1R}) & 0 & cos(\theta_{1R}) & a_0 + a_1 cos(\theta_{1R}) \\ cos(\pi - \theta_{1R}) & 0 & cos(\frac{\pi}{2} - \theta_{1R}) & a_1 sin(\theta_{1R}) \\ 0 & -1 & 0 & -d_1 \\ 0 & 0 & 0 & 1 \end{bmatrix}$$

(1)

$$T_{1R}^{2R} = \begin{bmatrix} cos(\theta_{2R}) & -sin(\theta_{2R}) & 0 & a_2cos(\theta_{2R}) \\ sin(\theta_{2R}) & cos(\theta_{2R}) & 0 & a_2sin(\theta_{2R}) \\ 0 & 0 & 1 & 0 \\ 0 & 0 & 0 & 1 \end{bmatrix} \quad (2)$$

$$T_{2R}^{3R} = \begin{bmatrix} cos(\theta_{3R} + \frac{\pi}{2}) & -sin(\theta_{3R} + \frac{\pi}{2}) & 0 & a_3cos(\theta_{3R}) \\ sin(\theta_{3R} + \frac{\pi}{2}) & cos(\theta_{3R} + \frac{\pi}{2}) & 0 & a_3sin(\theta_{3R}) \\ 0 & 0 & 1 & 0 \\ 0 & 0 & 0 & 1 \end{bmatrix} \quad (3)$$

$$T_{3R}^{4R} = \begin{bmatrix} cos(\theta_{4R}) & -sin(\theta_{4R}) & 0 & a_4cos(\theta_{4R}) \\ sin(\theta_{4R}) & cos(\theta_{4R}) & 0 & a_4sin(\theta_{4R}) \\ 0 & 0 & 1 & 0 \\ 0 & 0 & 0 & 1 \end{bmatrix} \quad (4)$$

Based on the derived homogeneous transformation matrices, the forward kinematics model for the right leg of the LLE can be formulated as follows:

$$\begin{aligned} T_0^{4R} &= T_0^{1R} T_{1R}^{2R} T_{2R}^{3R} T_{3R}^{4R} \\ &= \begin{bmatrix} -sin(\theta_{1R})sin(\Phi) & -sin(\theta_{1R})cos(\Phi) & cos(\theta_{1R}) & P_{xR} \\ cos(\theta_{1R})sin(\Phi) & cos(\theta_{1R})cos(\Phi) & sin(\theta_{1R}) & P_{yR} \\ -cos(\Phi) & sin(\Phi) & 0 & P_{zR} \\ 0 & 0 & 0 & 1 \end{bmatrix} \end{aligned} \quad (5)$$

where

$$\Phi = \theta_{2R} + \theta_{3R} + \theta_{4R} \quad (6)$$

and P_{xR}, P_{yR}, and P_{zR} denote the Cartesian coordinates of Frame 4R (O_{4R}), representing the right foot end-effector of the exoskeleton, in relation to Frame 0 (origin) along the X_0, Y_0, and Z_0 axes, respectively. These position are derived as:

$$P_{xR} = a_0 + a_1 cos(\theta_{1R}) + \mathcal{P} sin(\theta_{1R}) \quad (7)$$

$$P_{yR} = a_1 sin(\theta_{1R}) - \mathcal{P} cos(\theta_{1R}) \quad (8)$$

$$P_{zR} = -d_1 - a_2 sin(\theta_{2R}) - a_3 sin(\theta_{2R} + \theta_{3R}) - a_4 cos(\Phi) \quad (9)$$

where

$$\mathcal{P} = a_2 cos(\theta_{2R}) + a_3 cos(\theta_{2R} + \theta_{3R}) - a_4 sin(\Phi) \quad (10)$$

Hence, the orientation and position of the right foot end-effector (O_{4R}) with respect to the origin (O) can be formulated as follows:

$$R_0^{4R} = \begin{bmatrix} -sin(\theta_{1R})sin(\Phi) & -sin(\theta_{1R})cos(\Phi) & cos(\theta_{1R}) \\ cos(\theta_{1R})sin(\Phi) & cos(\theta_{1R})cos(\Phi) & sin(\theta_{1R}) \\ -cos(\Phi) & sin(\Phi) & 0 \end{bmatrix} \quad (11)$$

$$P_0^{4R} = \begin{bmatrix} P_{xR} \\ P_{yR} \\ P_{zR} \end{bmatrix} \quad (12)$$

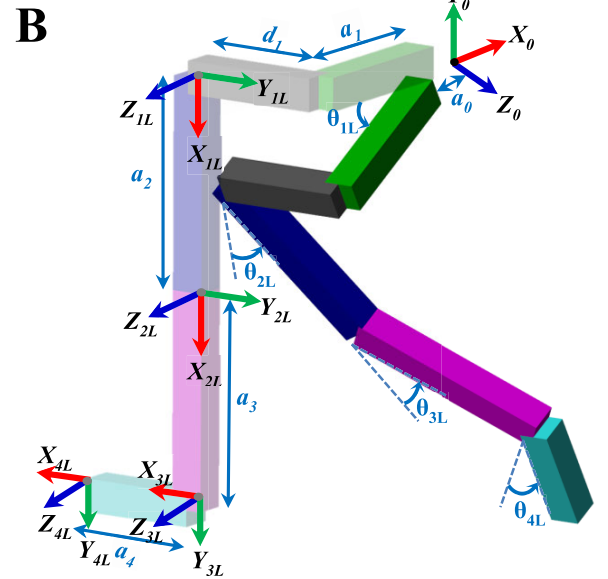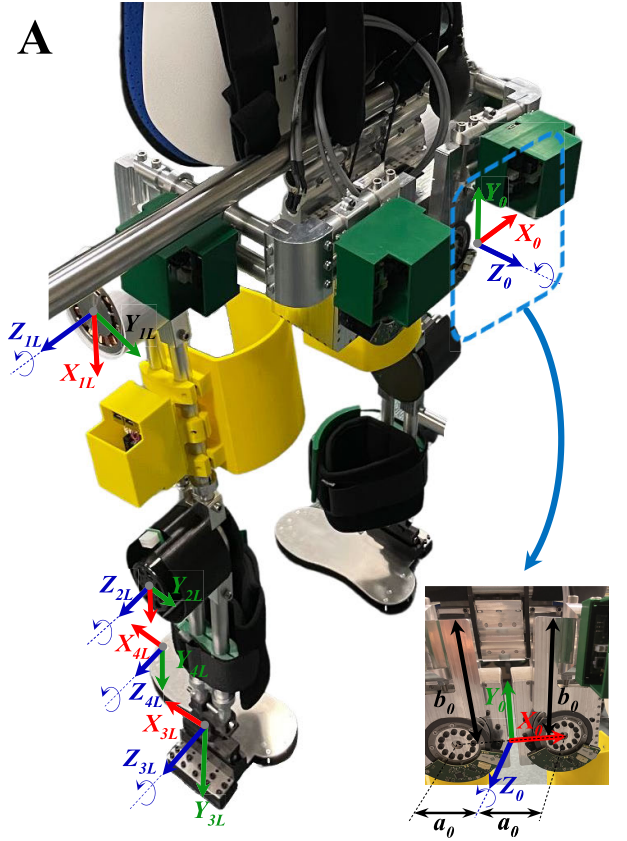**FIGURE 4.** Forward kinematic analysis of the left leg of the LLE. (A) The left leg of the LLE with assigned cartesian coordinate frames. (B) Dimensions of the simplified model of the left leg of the LLE.

B. LEFT LEG

In a similar scenario, Fig. 4A represents the Cartesian coordinate frames assigned to the left leg of the LLE. Subsequently, the simplified model dimensions of this leg are
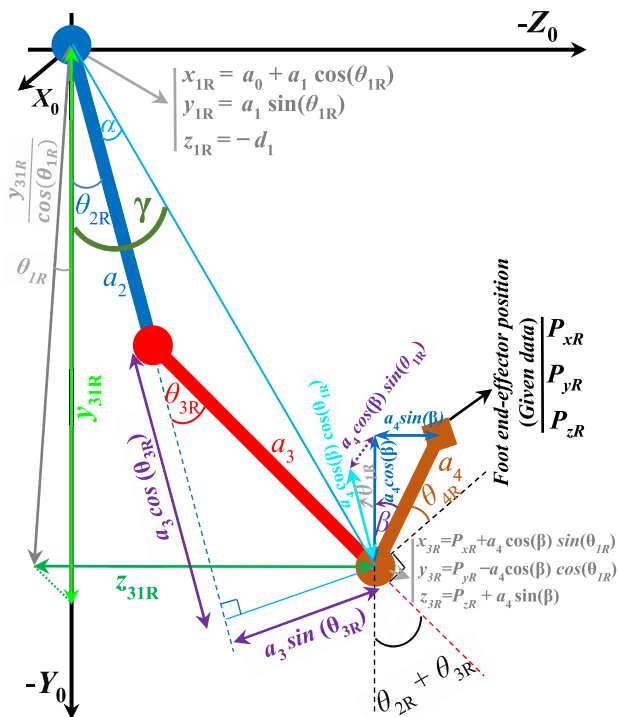
FIGURE 5. Geometry-driven inverse kinematics analysis of the LLE's right leg.

elucidated in Fig. 5B. Based on this Fig. and similar to the right leg, the resulting homogeneous transformation matrix for the left leg of the LLE can be derived as:

$$
T_0^{4L}
$$
$$
= \begin{bmatrix} sin(\theta_{1L})sin(\psi) & sin(\theta_{1L})cos(\psi) & -cos(\theta_{1L}) & P_{xL} \\ -cos(\theta_{1L})sin(\psi) & -cos(\theta_{1L})cos(\psi) & -sin(\theta_{1L}) & P_{yL} \\ -cos(\psi) & sin(\psi) & 0 & P_{zL} \\ 0 & 0 & 0 & 1 \end{bmatrix}
$$
$$(13)$$

where

$$\psi = \theta_{2L} + \theta_{3L} + \theta_{4L} \tag{14}$$

and P_{xL}, P_{yL}, and P_{zL} represent the Cartesian coordinates of Frame 4L (O_{4L}), which corresponds to the left foot end-effector of the exoskeleton, relative to Frame 0 (origin) along the X_0, Y_0, and Z_0 axes, respectively. The positions are derived as follows:

$$P_{xL} = -a_0 - a_1 cos(\theta_{1L}) + \mathcal{H}sin(\theta_{1L}) \tag{15}$$
$$P_{yL} = -a_1 sin(\theta_{1L}) - \mathcal{H}cos(\theta_{1L}) \tag{16}$$
$$P_{zL} = -d_1 + a_2 sin(\theta_{2L}) + a_3 sin(\theta_{2L} + \theta_{3L}) - a_4 cos(\psi) \tag{17}$$

where

$$\mathcal{H} = a_2 cos(\theta_{2L}) + a_3 cos(\theta_{2L} + \theta_{3L}) + a_4 sin(\psi) \tag{18}$$

Consequently, the orientation and position of the left foot end-effector (O_{4L}) with respect to the origin (O) can be expressed as follows:

$$
R_0^{4L} = \begin{bmatrix} sin(\theta_{1L})sin(\psi) & sin(\theta_{1L})cos(\psi) & -cos(\theta_{1L}) \\ -cos(\theta_{1L})sin(\psi) & -cos(\theta_{1L})cos(\psi) & -sin(\theta_{1L}) \\ -cos(\psi) & sin(\psi) & 0 \end{bmatrix}
$$
$$(19)$$

$$
P_0^{4L} = \begin{bmatrix} P_{xL} \\ P_{yL} \\ P_{zL} \end{bmatrix} \tag{20}
$$

IV. INVERSE KINEMATICS

Inverse kinematics calculates the required joint angles to achieve a specific end-effector position and orientation [33]. Due to its reliance on inverse trigonometric functions, inverse kinematics often yields multiple solutions in robotics, reflecting its non-unique solution nature. An ordinary resolution strategy integrates robot structural properties and actual pose. Existing literature confirms that an analytical solution to the inverse kinematics problem is derivable for kinematic chains with five or fewer DOFs. In these instances, joint angles can be calculated algebraically [23], [33], [37]. In the inverse kinematic analysis for each leg, the desired orientation (R_0^4) and desired Cartesian position (P_0^4) of each foot end-effector (Frame 4) with respect to the origin are assumed to be provided. The objective is to derive the angular revolute joint parameters, θ_1, θ_2, θ_3, and θ_4, for each foot.

A. RIGHT LEG

As the desired orientation (R_0^{4R}) is provided in (11), $sin(\theta_{1R})$ and $sin(\Phi)$ can be directly obtained from $R_0^{4R}(2, 3)$ and $R_0^{4R}(3, 2)$, respectively. Consequently, θ_{1R} and Φ can be derived as follows:

$$\theta_{1R} = sin^{-1}(sin(\theta_{1R})) \tag{21}$$
$$\Phi = sin^{-1}(sin(\Phi)) \tag{22}$$

For real values of X within the range $[-1, 1]$, the inverse sine function, $sin^{-1}(X)$, returns values in the interval $[-\pi/2, \pi/2]$. Consequently, θ_{1R} and Φ must lie between $-\pi/2$ and $\pi/2$, which is fully compatible with the motion restrictions of the human body. By squaring (7) and (8), the following expressions are obtained:

$$(a_1 cos(\theta_{1R}))^2 + (\mathcal{P}sin(\theta_{1R}))^2 + 2a_1\mathcal{P}cos(\theta_{1R})sin(\theta_{1R})$$
$$= (P_{xR} - a_0)^2 \tag{23}$$
$$(a_1 sin(\theta_{1R}))^2 + (\mathcal{P}cos(\theta_{1R}))^2 - 2a_1\mathcal{P}cos(\theta_{1R})sin(\theta_{1R})$$
$$= P_{yR}^2 \tag{24}$$

Upon adding (23) and (24) together, the parameter of P can be derived as follows:

$$\mathcal{P} = \pm\sqrt{(P_{xR} - a_0)^2 + P_{yR}^2 - a_1^2} \tag{25}$$

Drawing from equation (10) and taking into account that a_2 and a_3 exceed a_4, as well as the constraint that the arguments

of trigonometric functions fall within the interval of $-\pi/2$ to $\pi/2$, it is concluded that only the positive solution for $\mathcal{P}$ is acceptable. Consequently, $\mathcal{P}$ is updated as follows:

$$\mathcal{P} = \sqrt{(P_{xR} - a_0)^2 + P_{yR}^2 - a_1^2} \tag{26}$$

Taking into account (9) and (10), the following relationship is established:

$$a_2 sin(\theta_{2R}) + a_3 sin(\theta_{2R} + \theta_{3R}) = \mathcal{A} \tag{27}$$
$$a_2 cos(\theta_{2R}) + a_3 cos(\theta_{2R} + \theta_{3R}) = \mathcal{B} \tag{28}$$

where

$$\mathcal{A} = -P_{zR} - d_1 - a_4 cos(\Phi) \tag{29}$$
$$\mathcal{B} = \mathcal{P} + a_4 sin(\Phi) \tag{30}$$

By squaring (27) and (28) and subsequently adding them, the resulting expressions are obtained:

$$a_2^2 + a_3^2 + 2a_2 a_3 cos(\theta_{3R}) = \mathcal{A}^2 + \mathcal{B}^2 \tag{31}$$

Based on equation (31), the parameter of θ_{3R} can be determined as follows:

$$\theta_{3R} = \pm cos^{-1}(\frac{\mathcal{A}^2 + \mathcal{B}^2 - a_2^2 - a_3^2}{2a_2 a_3}) \tag{32}$$

Given that θ_{3R} corresponds to the angular position of the exoskeleton's knee joint, the negative solution is the only acceptable option. As a result, the updated expression for θ_{3R} is formulated as follows:

$$\theta_{3R} = -cos^{-1}(\frac{\mathcal{A}^2 + \mathcal{B}^2 - a_2^2 - a_3^2}{2a_2 a_3}) \tag{33}$$

in this context, $\mathcal{A}$ and $\mathcal{B}$ are extracted from (29) and (30), while the parameter $\mathcal{P}$ is obtained from equation (26).

Fig. 5 illustrates the geometry-driven inverse kinematics analysis for the LLE's right leg, which aids in determining the parameter of θ_{2R}. This Fig. demonstrates that:

$$\theta_{2R} = \gamma - \alpha \tag{34}$$

where

$$\gamma = tan^{-1}\left(\frac{z_{31R}}{\frac{y_{31R}}{cos(\theta_{1R})}}\right) = tan^{-1}\left(\frac{cos(\theta_{1R})(z_{3R} - z_{1R})}{(y_{3R} - y_{1R})}\right)$$
$$= tan^{-1}\left(\frac{cos(\theta_{1R})(P_{zR} + a_4 sin(\beta) + d_1)}{P_{yR} - a_4 cos(\beta) cos(\theta_{1R}) - a_1 sin(\theta_{1R})}\right) \tag{35}$$

$$\alpha = tan^{-1}\left(\frac{a_3 sin(\theta_{3R})}{a_2 + a_3 cos(\theta_{3R})}\right) \tag{36}$$

$$\beta = \frac{\pi}{2} - \Phi \tag{37}$$

Utilizing (34)-(37), which stem from a unique and innovative geometric solution, θ_{2R} can be directly determined based on the given and known parameters. Ultimately, θ_{4R} can be calculated using (6) as follows:

$$\theta_{4R} = \Phi - \theta_{2R} - \theta_{3R} \tag{38}$$

where θ_{2R} and θ_{3R} have been determined using the preceding equations.

B. LEFT LEG

As indicated by the provided desired orientation (R_0^{4L}) in (19), $sin(\theta_{1L})$ and $sin(\psi)$ can be directly obtained from $R_0^{4L}(2, 3)$ and $R_0^{4L}(3, 2)$, respectively. As a result, θ_{1L} and ψ can be derived as follows:

$$R_0^{4L}(2, 3) = -sin(\theta_{1L}) \Rightarrow \theta_{1L} = sin^{-1}(-R_0^{4L}(2, 3)) \tag{39}$$

$$R_0^{4L}(3, 2) = sin(\psi) \Rightarrow \psi = sin^{-1}(R_0^{4L}(3, 2)) \tag{40}$$

For real values of X falling within the range $[-1, 1]$, the inverse sine function, $sin^{-1}(X)$, yields values in the interval $[-\pi/2, \pi/2]$. As a result, θ_{1L} and ψ must reside between $-\pi/2$ and $\pi/2$, aligning with the motion limitations of the human body. Similar to the right leg, by squaring equations (15) and (16) and considering that $\mathcal{H}$ is positive according to equation (18), the following expressions can be derived:

$$\mathcal{H} = \sqrt{(P_{xL} + a_0)^2 + P_{yL}^2 - a_1^2} \tag{41}$$

Considering equations (17) and (18), the following relationship can be established:

$$a_2 sin(\theta_{2L}) + a_3 sin(\theta_{2L} + \theta_{3L}) = \mathcal{C} \tag{42}$$
$$a_2 cos(\theta_{2L}) + a_3 cos(\theta_{2L} + \theta_{3L}) = \mathcal{D} \tag{43}$$

where

$$\mathcal{C} = P_{zL} + d_1 + a_4 cos(\psi) \tag{44}$$
$$\mathcal{D} = \mathcal{H} - a_4 sin(\psi) \tag{45}$$

By squaring (42) and (43), then adding them together, and taking into account that θ_{3L}, which is related to the exoskeleton's left knee joint, must have a positive value, the following result can be derived:

$$\theta_{3L} = cos^{-1}(\frac{\mathcal{C}^2 + \mathcal{D}^2 - a_2^2 - a_3^2}{2a_2 a_3}) \tag{46}$$

where $\mathcal{C}$ and $\mathcal{D}$ are taken from (44) and (45), while the parameter $\mathcal{H}$ is extracted from (41). It is important to note that, owing to the restrictions of the inverse cosine function (cos^{-1}), the angle θ_{3L} must fall within the range of $-\pi/2$ to $\pi/2$. Moreover, given that the angle should be positive, the final range for θ_{3L} should be between 0 and $\pi/2$.

Fig. 6 depicts the geometry-driven inverse kinematics analysis for the left leg of the LLE, which assists in determining the parameter θ_{2L}. This illustration presents the following:

$$\theta_{2L} = \lambda - \delta \tag{47}$$

where

$$\lambda = tan^{-1}\left(\frac{-z_{31L}}{\frac{y_{31L}}{cos(\theta_{1L})}}\right) = tan^{-1}\left(\frac{-cos(\theta_{1L})(z_{3L} - z_{1L})}{(y_{3L} - y_{1L})}\right)$$
$$= tan^{-1}\left(\frac{-cos(\theta_{1L})(P_{zL} + a_4 sin(\eta) + d_1)}{P_{yL} - a_4 cos(\eta) cos(\theta_{1L}) - a_1 sin(\theta_{1L})}\right) \tag{48}$$
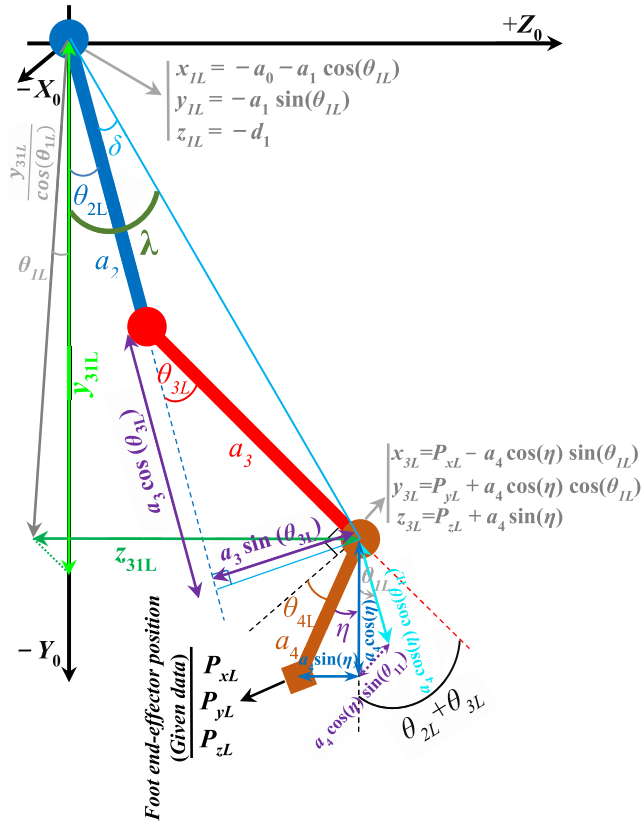
FIGURE 6. Geometry-driven inverse kinematics analysis of the LLE's left leg.

$$\delta = \tan^{-1}\left(\frac{a_3\sin(\theta_{3R})}{a_2 + a_3\cos(\theta_{3R})}\right) \quad (49)$$

$$\eta = \frac{\pi}{2} - \psi \quad (50)$$

Given that Z_0 has a positive direction and Y_0 has a negative direction, in (48), z_{31L} is multiplied by a negative value to align the directions consistently. Employing (47)-(50), which originate from a distinctive and novel geometric approach, θ_{2L} can be directly derived based on the provided and known parameters. Consequently, θ_{4L} can be computed using equation (14) as follows:

$$\theta_{4L} = \psi - \theta_{2L} - \theta_{3L} \quad (51)$$

where θ_{2L} and θ_{3L} are ascertained using the previously mentioned equations.

V. SIMULATION RESULTS AND DISCUSSION
This paper uses a Simulink-Simscape model for validating and verifying the kinematic analysis depicted in Fig. 7A. Simscape Multibody™ was utilized to represent the forward kinematics of a simplified model for each leg within the Simscape™ environment (Fig. 7B). As Fig. 7B shows, the desired angular positions inputted into the Simscape model were digitized and processed using a 2nd order low-pass filter, devoid of lag, with a 1 ms filtering time constant. To model both forward and inverse kinematics
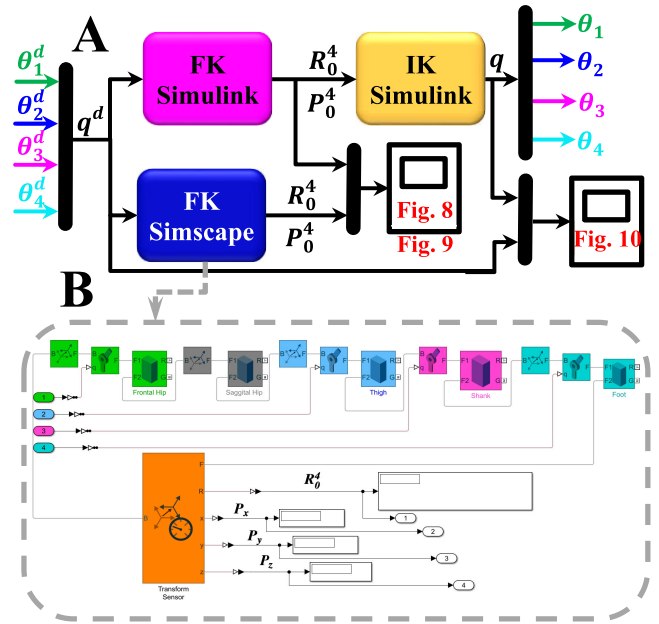

FIGURE 7. (A) Validation of forward kinematics (FK) through a comparative approach involving simscape and simulink models, followed by kinematic verification using sequential forward and inverse kinematics (IK) analyses. (B) Inside the FK simscape model.

in Simulink, one MATLAB Function has been employed for each. Using the formulations provided in the previous sections, these MATLAB Functions utilize MATLAB code to accurately represent the kinematic behavior of the LLE system. Fig. 7A shows that forward kinematics is validated through a comparison using Simscape™ and Simulink® simulations. Subsequently, a sequential forward and inverse kinematics analysis is conducted to verify the kinematic analysis. For the simulation purpose and based on Fig. 3 and Fig. 4, the values assigned to each parameter are as follows: a_0 is equivalent to 0.025m, a_1 is 0.15m, d_1 is 0.2135m, a_2 is 0.32m, a_3 is 0.325m, and a_4 is determined to be 0.235m. This study employed a standard gait trajectory as the desired trajectory. The simulation was conducted using MATLAB R2021a and extended over a duration of 30 seconds. A supplementary video is provided alongside this paper to enhance understanding and offer readers a visual insight into the subject. This video is organized into two distinct segments: the initial part meticulously elucidates the design of the LLE, while the subsequent section demonstrates the LLE's motion in accordance with the provided gait pattern. Additionally, a supplementary simulation file named "Kinematic_Analysis.slx," provided with this paper and developed in MATLAB R2021a, is used to simulate the kinematic analysis of both legs of the LLE.

Fig. 8 and Fig. 9 validate the forward kinematics, respectively, for the right and left leg of the LLE through a comparative analysis of simulations from Simscape™ and Simulink®, focusing on the rotation matrix (R_0^4) and the translation vector (P_0^4). The difference between the Simscape and Simulink results for both the rotation matrix and
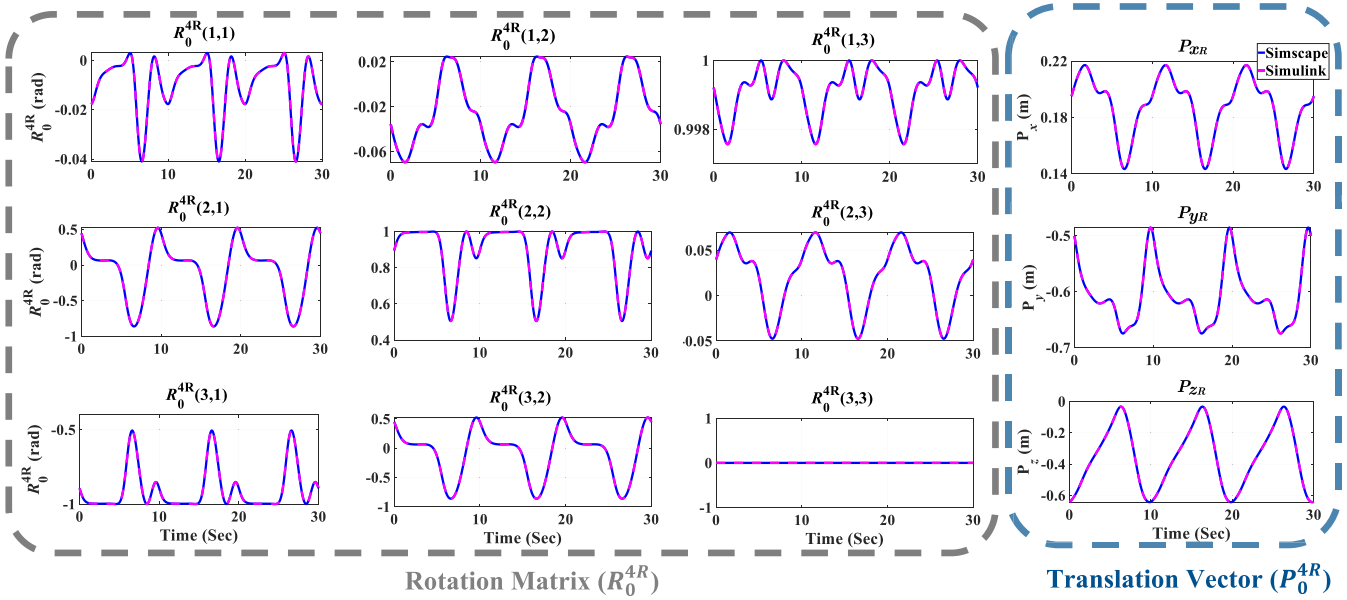
FIGURE 8. Validation of forward kinematics for the LLE's right leg with a comparative analysis of simscape and simulink simulations.
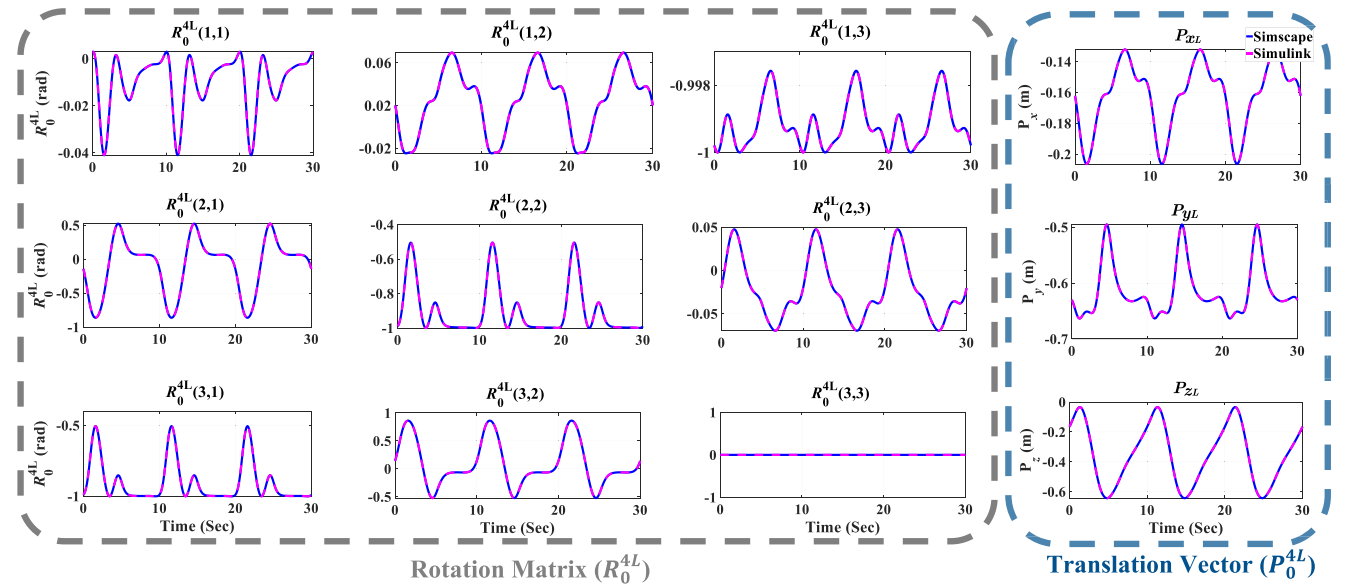

FIGURE 9. Validation of forward kinematics for the LLE's left leg with a comparative analysis of simscape and simulink simulations.

translation vector falls within the range of 10^{-3} degree, a result attributable to the second-order filtering time constant (0.001) used in the Simscape model. This level of discrepancy attests to the validity and accuracy of the derived forward kinematic model for both the right and left legs.

Fig. 10 verifies the kinematic analysis of the right and left legs by comparing the desired trajectory $\left(q^d = \left[\theta_1^d, \theta_2^d, \theta_3^d, \theta_4^d\right]\right)$, which is the input to the forward kinematics, with the output from the inverse kinematics ($q = [\theta_1, \theta_2, \theta_3, \theta_4]$). This Fig. shows that q closely tracks q^d under a standard and smooth gait pattern with a gait cycle

of 10 sec. In this Fig., θ_{Le} and θ_{Re} show the discrepancy between q^d and q for the right and left leg, which are at the range of 10^{-12} degree. This range verifies the accuracy of both forward kinematics and inverse kinematics for both legs. The extremely tiny discrepancy arises from the numerical precision and solver settings in the simulation environment. Figs. 8 and 9 demonstrate that $R_0^{4R}(3, 3)$ and $R_0^{4L}(3, 3)$ are zero throughout the entire simulation time. This is because Z_0^{4R} and Z_0^{4L} are perpendicular to Z_0, regardless of the rotation angles, as illustrated in Figs. 3 and 4. This issue can also be observed in (11) and (19), where $R_0^{4R}(3, 3)$ and $R_0^{4L}(3, 3)$ are
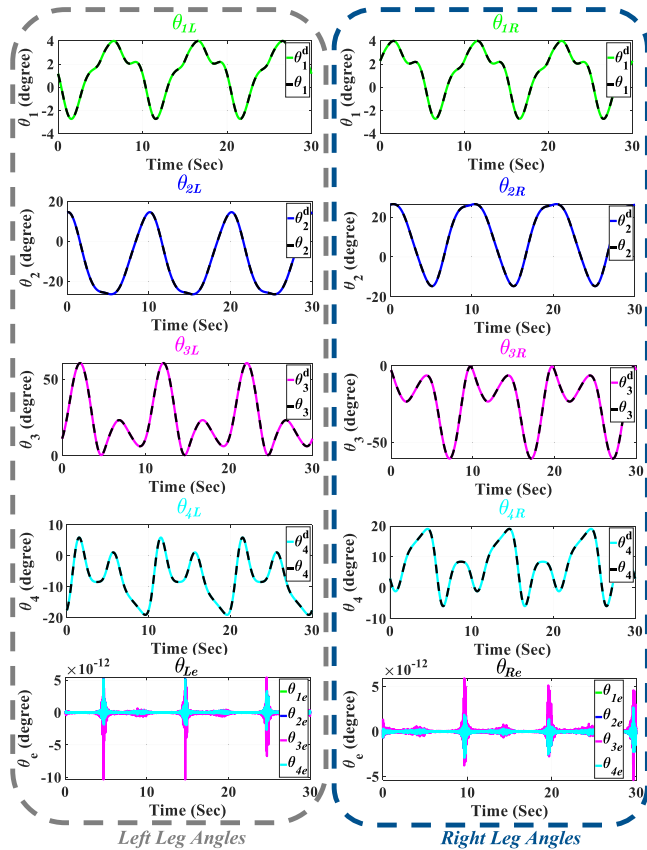
FIGURE 10. Kinematic verification for the LLE through sequential forward and inverse kinematics analyses.

zero. Moreover, Eqs. (11) and (19) clarify that $R_0^{4R}(3, 2) = \sin(\Phi)$ and $R_0^{4L}(3, 2) = \sin(\psi)$, where $\Phi = \theta_{2R} + \theta_{3R} + \theta_{4R}$ and $\psi = \theta_{2L} + \theta_{3L} + \theta_{4L}$, respectively.

In Figs. 8 and 9, the values of $R_0^{4R}(3, 2)$ and $R_0^{4L}(3, 2)$ fluctuate between the ranges of [0.5, -0.866] and [-0.5, 0.866], respectively. This indicates that the angles Φ and ψ vary within $[30°, -60°]$ and $[-30°, 60°]$, respectively, in the sagittal plane. This fluctuation range for the left and right legs can be clearly observed in Fig. 10, where the angles $-60°$ and $60°$ can be seen in θ_{3R} and θ_{3L}, respectively. Furthermore, Fig. 10 implies that $\theta_{2R} + \theta_{3R} + \theta_{4R}$ and $\theta_{2L} + \theta_{3L} + \theta_{4L}$ consistently remain within the bounds of $[30°, -60°]$ and $[-30°, 60°]$, respectively. Moreover, from Eqs. (11) and (19), it can be found that $R_0^{4R}(1, 3) = \cos(\theta_{1R})$ and $R_0^{4L}(1, 3) = -\cos(\theta_{1L})$, respectively. The values of the $R_0^{4R}(1, 3)$ and $R_0^{4L}(1, 3)$ depicted in Fig. 8 and Fig. 9 indicate that θ_{1R} and θ_{1L} are approximately zero, with minimal fluctuations, which is consistent with the findings presented in Fig. 10.

Eqs. (7) and (15) describe the relationships $P_{xR} = a_0 + a_1 \cos(\theta_{1R}) + \mathcal{P} \sin(\theta_{1R})$ and $P_{xL} = -a_0 - a_1 \cos(\theta_{1L}) + \mathcal{H} \sin(\theta_{1L})$, respectively. Based on Fig. 10, where θ_{1R} and θ_{1L} are shown as small values approximating zero, we can use the small-angle approximations for sine and cosine. Consequently, the relationships simplify to $P_{xR} \approx a_0 + a_1$ and $P_{xL} \approx -a_0 - a_1$, with minimal fluctuations. Given that

$a_0 = 0.025$m and $a_1 = 0.15$m, the expected average values for P_{xR} and P_{xL} are 0.175m and -0.175m, respectively. These values are subject to tiny fluctuations, consistent with the behavior of θ_{1R} and θ_{1L} as depicted in Fig. 10. Furthermore, it becomes apparent that P_{xR} and P_{xL} follow trajectories similar to those of θ_{1R} and θ_{1L}, but with a magnified amplitude. This observation strengthens the conclusion that the trajectories of P_{xR} and P_{xL} are intrinsically linked to the rotations of θ_{1R} and θ_{1L}, respectively. From Figs. 8 and 9, it can be observed that P_{yR} and P_{yL}, as well as P_{zR} and P_{zL}, follow similar trajectories. The only difference between them is a half-gait cycle delay which is 5 seconds in this study.

VI. CONCLUSION

The present study developed a unique LLE featuring size adjustability specifically tailored to accommodate children aged 8 to 12. A comprehensive analysis of body measurements was conducted to ensure a proper fit across the varied physical dimensions characteristic of this age group. The design incorporated Brushless DC motors and Harmonic Drive gears, selected for superior efficiency. Additionally, the EtherCAT communication protocol was implemented to facilitate high-frequency operation, enhancing the responsiveness of the exoskeleton. Furthermore, the study includes a detailed forward kinematic analysis for each leg of the exoskeleton. This is complemented by an advanced algebraic-geometrical solution for the inverse kinematic analysis of each leg of the exoskeleton. It further offers a specific validation and verification strategy for kinematic analysis. For each leg, the rotation matrix and translation vector are compared across two independent environments—Simscape™ and Simulink®—to validate the forward kinematics. Additionally, the desired trajectory is contrasted with the inverse kinematic outputs to verify the kinematic analysis, with the forward and inverse kinematics arranged sequentially. The convergence of results from both forward and inverse kinematic analyses fully validates and verifies the kinematic analysis for both legs of the LLE, providing a sturdy groundwork for the effective control of the LLE.

LIMITATIONS AND FUTURE WORK

A primary limitation of this pediatric LLE is its design tailored specifically for children aged 8 to 12, making it unsuitable for other age groups. Adapting to the swift developmental transitions in this age bracket, both physically and cognitively, presents a significant challenge for this assistive tool. While the device is constructed from lightweight materials, optimizing its weight and size is essential to ensure lasting comfort, especially considering children's unique sensitivity and adaptability. Real-time processing and response are crucial in pediatric robotic exoskeletons. Latency or software inconsistencies could result in suboptimal performance or, in severe cases, potential accidents.

In this study, the LLE operated in an unpowered mode, limiting the analysis to simulation-based kinematics. Future research will present experimental results for comparison with these simulation findings. In future research, the LLE will be mounted to a frame. Using the kinematic analysis from this study, the dynamic model of the mounted LLE, both with and without a child-sizer dummy, will be derived. Subsequently, upon unmounting the LLE, a controller will be established to facilitate a child's walk with the LLE in two distinct modes: (i) passive user, where the user exerts no force, and (ii) active user, where the user exerts force, based on the previously derived dynamic model. The differential outcomes between active and passive modes will shape the human-LLE interaction control to be detailed in upcoming studies.

ACKNOWLEDGMENT

REFERENCES

[1] M. A. Alexander, J. M. Dennis, and K. P. Murphy, *Pediatric Rehabilitation: Principles and Practice*, 5th ed. New York, NY, USA: Demos Medical Publishing, 2015.

[2] P. Rosenbaum, N. Paneth, A. Leviton, M. Goldstein, and M. Bax, "A report: The definition and classification of cerebral palsy April 2006," *Dev. Med. Child Neurol.*, vol. 49, no. 109, pp. 8–14, 2007.

[3] M. L. Aisen, D. Kerkovich, J. Mast, S. Mulroy, T. A. Wren, R. M. Kay, and S. A. Rethlefsen, "Cerebral palsy: Clinical care and neurological rehabilitation," *Lancet Neurol.*, vol. 10, no. 9, pp. 844–852, Sep. 2011.

[4] Centers for Disease Control and Prevention. (May 2, 2022). *Data and Statistics for Cerebral Palsy*. Centers for Disease Control and Prevention. Accessed: Aug. 11, 2023. [Online]. Available: https://www.cdc.gov/ncbddd/cp/data.html

[5] D. Duan, N. Goemans, S. Takeda, E. Mercuri, and A. Aartsma-Rus, "Duchenne muscular dystrophy," *Nature Rev. Disease Primers*, vol. 7, no. 1, pp. 1–19, Feb. 2021.

[6] M. R. Lunn and C. H. Wang, "Spinal muscular atrophy," *Lancet*, vol. 371, no. 9630, pp. 2120–2133, Jun. 2008.

[7] K. J. Swoboda, "Seize the day: Newborn screening for SMA," *Amer. J. Med. Genet. A*, vol. 152A, no. 7, pp. 1605–1607, Jun. 2010.

[8] S. Parent, J.-M. Mac-Thiong, M. Roy-Beaudry, J. F. Sosa, and H. Labelle, "Spinal cord injury in the pediatric population: A systematic review of the literature," *J. Neurotrauma*, vol. 28, no. 8, pp. 1515–1524, Aug. 2011.

[9] K. F. Bjornson, B. Belza, D. Kartin, R. Logsdon, and J. F. McLaughlin, "Ambulatory physical activity performance in youth with cerebral palsy and youth who are developing typically," *Phys. Therapy*, vol. 87, no. 3, pp. 248–257, Mar. 2007.

[10] E. R. John, L. Prichep, H. Ahn, P. Easton, J. Fridman, and H. Kaye, "Neurometric evaluation of cognitive dysfunctions and neurological disorders in children," *Prog. Neurobiol.*, vol. 21, no. 4, pp. 239–290, Jan. 1983.

[11] L. Mutch, E. Alberman, B. Hagberg, K. Kodama, and M. V. Perat, "Cerebral palsy epidemiology: Where are we now and where are we going?" *Develop. Med. Child Neurol.*, vol. 34, no. 6, pp. 547–551, Nov. 2008.

[12] G. Orekhov, Y. Fang, J. Luque, and Z. F. Lerner, "Ankle exoskeleton assistance can improve over-ground walking economy in individuals with cerebral palsy," *IEEE Trans. Neural Syst. Rehabil. Eng.*, vol. 28, no. 2, pp. 461–467, Feb. 2020.

[13] M. O. Bair, *The Design and Testing of a Powered Exoskeleton to Reduce the Metabolic Cost of Walking in Individuals With Cerebral Palsy*. Flagstaff, AZ, USA: northern Arizona Univ., May 2018.

[14] M. Sarajchi, M. K. Al-Hares, and K. Sirlantzis, "Wearable lower-limb exoskeleton for children with cerebral palsy: A systematic review of mechanical design, actuation type, control strategy, and clinical evaluation," *IEEE Trans. Neural Syst. Rehabil. Eng.*, vol. 29, pp. 2695–2720, Dec. 2021.

[15] *Neurological Disorders: Public Health Challenges*, WHO, World Health Organization, Geneva, Switzerland, 2006.

[16] H. Yali and W. Xingsong, "Kinematics analysis of lower extremity exoskeleton," in *Proc. Chin. Control Decis. Conf.*, Jul. 2008, pp. 2837–2842.

[17] R. M. Andrade, S. Sapienza, and P. Bonato, "Development of a 'transparent operation mode' for a lower-limb exoskeleton designed for children with cerebral palsy," in *Proc. IEEE 16th Int. Conf. Rehabil. Robot. (ICORR)*, Jun. 2019, pp. 512–517.

[18] D. Zanotto, Y. Akiyama, P. Stegall, and S. K. Agrawal, "Knee joint misalignment in exoskeletons for the lower extremities: Effects on user's gait," *IEEE Trans. Robot.*, vol. 31, no. 4, pp. 978–987, Aug. 2015.

[19] M. Cempini, S. M. M. De Rossi, T. Lenzi, N. Vitiello, and M. C. Carrozza, "Self-alignment mechanisms for assistive wearable robots: A kinetostatic compatibility method," *IEEE Trans. Robot.*, vol. 29, no. 1, pp. 236–250, Feb. 2013.

[20] R. Kolaghassi, G. Marcelli, and K. Sirlantzis, "Deep learning models for stable gait prediction applied to exoskeleton reference trajectories for children with cerebral palsy," *IEEE Access*, vol. 11, pp. 31962–31976, 2023.

[21] A. Zeiaee, R. Soltani-Zarrin, R. Langari, and R. Tafreshi, "Design and kinematic analysis of a novel upper limb exoskeleton for rehabilitation of stroke patients," in *Proc. Int. Conf. Rehabil. Robot. (ICORR)*, Jul. 2017, pp. 759–764.

[22] M. Sarajchi and K. Sirlantzis, "Design and control of a single-leg exoskeleton with gravity compensation for children with unilateral cerebral palsy," *Sensors*, vol. 23, no. 13, pp. 1–35, Jul. 2023.

[23] X. Zhang, H. Wang, Y. Tian, L. Peyrodie, and X. Wang, "Model-free based neural network control with time-delay estimation for lower extremity exoskeleton," *Neurocomputing*, vol. 272, pp. 178–188, Jan. 2018.

[24] M. Lyu, W. Chen, X. Ding, J. Wang, S. Bai, and H. Ren, "Design of a biologically inspired lower limb exoskeleton for human gait rehabilitation," *Rev. Sci. Instrum.*, vol. 87, no. 10, Oct. 2016, Art. no. 104301.

[25] J. Li, J. Peng, Z. Lu, and K. Huang, "The wearable lower limb rehabilitation exoskeleton kinematic analysis and simulation," *BioMed Res. Int.*, vol. 2022, pp. 1–10, Aug. 2022.

[26] Y. Zhang, M. Bressel, S. De Groof, F. Dominé, L. Labey, and L. Peyrodie, "Design and control of a size-adjustable pediatric lower-limb exoskeleton based on weight shift," *IEEE Access*, vol. 11, pp. 6372–6384, 2023.

[27] R. M. Malina, P. V. Hamill, and S. Lemeshow, *Selected Body Measurements of Children 6–11 Years, United States*. Hyattsville, MD, USA: National Center for Health Statistics, Jan. 1973.

[28] E. Whitley, D. Gunnell, G. Davey Smith, J. M. P. Holly, and R. M. Martin, "Childhood circumstances and anthropometry: The boyd orr cohort," *Ann. Hum. Biol.*, vol. 35, no. 5, pp. 518–534, Jul. 2009.

[29] C. D. Fryar, Q. Gu, and C. L. Ogden, *Anthropometric Reference Data for Children and Adults; United States, 2007–2010*. Atlanta, GA, USA: Centers for Disease Control and Prevention, Oct. 2012. Accessed: Aug. 2023. [Online]. Available: https://stacks.cdc.gov/view/cdc/12223

[30] S. Õunpuu, R. B. Davis, and P. A. DeLuca, "Joint kinetics: Methods, interpretation and treatment decision-making in children with cerebral palsy and myelomeningocele," *Gait Posture*, vol. 4, no. 1, pp. 62–78, Jan. 1996.

[31] D. Oeffinger, B. Brauch, S. Cranfill, C. Hisle, C. Wynn, R. Hicks, and S. Augsburger, "Comparison of gait with and without shoes in children," *Gait Posture*, vol. 9, no. 2, pp. 95–100, May 1999.

[32] T. H. Baluch, A. Masood, J. Iqbal, U. Izhar, and U. S. Khan, "Kinematic and dynamic analysis of a lower limb exoskeleton," *Int. J. Mech. Mechatron. Eng.*, vol. 6, no. 9, pp. 1945–1949, Sep. 2012.

[33] M. W. Spong, S. Hutchinson, and M. Vidyasagar, *Robot Modeling and Control*. New York, NY, USA: Wiley, Dec. 2006.

[34] C. Bayón, O. Ramírez, J. I. Serrano, M. D. D. Castillo, A. Pérez-Somarriba, J. M. Belda-Lois, I. Martínez-Caballero, S. Lerma-Lara, C. Cifuentes, A. Frizera, and E. Rocon, "Development and evaluation of a novel robotic platform for gait rehabilitation in patients with cerebral palsy: CPWalker," *Robot. Auto. Syst.*, vol. 91, pp. 101–114, May 2017.

[35] D. Yilmaz and A. A. Dehghani-Sanij, "A review of assistive robotic exoskeletons and mobility disorders in children to establish requirements of such devices for paediatric population," in *Proc. Mechatronics*, Glasgow, U.K., Jul. 2019, pp. 1–14.

[36] J. Denavit and R. S. Hartenberg, "A kinematic notation for lower-pair mechanisms based on matrices," *J. Appl. Mech.*, vol. 22, no. 2, pp. 215–221, Jun. 1955.

[37] K. M. Lynch and F. C. Park, *Modern Robotics: Mechanics, Planning, and Control*. Cambridge, U.K.: Cambridge Univ. Press, May 2017.

MOHAMMADHADI SARAJCHI (Student Member, IEEE) received the B.Sc. and M.Sc. degrees (Hons.) in electronic engineering. He is currently pursuing the Ph.D. degree with the School of Engineering, University of Kent. His academic journey includes being a Visiting Scholar with JUNIA-HEI, in 2022, and a Researcher with the Royal Holloway University of London, from 2018 to 2019. He also spent time as a Visiting Scholar with the Mechanical Engineering Department, Tsinghua University, in 2017. Since 2023, he has been engaged as a Graduate Research Assistant with the School of Engineering, Technology and Design, Canterbury Christ Church University (CCCU). He is a Graduate Teaching Assistant with the School of Engineering, University of Kent. His research interests include robotic control, physical human–robot interaction, and lower limb exoskeletons, contributing to significant advancements within these areas. He received the IET Postgraduate Research Award, in 2023.

KONSTANTINOS SIRLANTZIS is currently a Professor of applied artificial intelligence with the School of Engineering, Technology and Design, Canterbury Christ Church University (CCCU), Canterbury, Kent, U.K. Previously, he was an Associate Professor of intelligent systems with the School of Engineering, University of Kent, where he was the Head of the Robotics and Assistive Technologies Research Group and the Founding Director of the Kent Assistive RObotics Laboratory (KAROL). He has a strong track record in artificial intelligence and neural networks for image analysis and understanding, and robotic systems, with an emphasis on assistive technologies and pattern recognition for biometrics-based security applications. He has authored over 130 peer-reviewed papers in journals and conferences. He has organized and chaired a range of international conferences and workshops.

● ● ●